Microfluid Nanofluid (2014) 16:109–122
DOI 10.1007/s10404-013-1228-3

RESEARCH PAPER

Laser-induced fluorescence visualization of ion transport in a pseudo-porous capacitive deionization microstructure

Onur N. Demirer · Carlos H. Hidrovo

Received: 13 March 2013 / Accepted: 25 June 2013 / Published online: 9 July 2013

Abstract In this paper, a microfluidic experimental set-up is introduced to study the ionic transport in an artificial capacitive deionization (CDI) cell. CDI is a promising desalination technique, which relies on the application of an external electric field and high surface area porous electrodes for ion separation and storage. Photolithography and deep reactive ion etching were used to fabricate a micro-CDI channel with pseudo-porous electrodes on a silicon-on-insulator substrate. Laser-induced fluorescence was performed using cationic Sulforhodamine B (SRB) fluorescent dye to measure ion concentration within the bulk solution and more importantly, within the porous electrodes during the desalination process, with an average normalized root mean square deviation of 8.2 %. Using this set-up, electromigration of ions within the electrode was visualized and the effect of applied electric potential on bulk solution concentration distribution is quantified. In addition, SRB and Fluorescein were used together to visualize anion and cation concentrations simultaneously. The method presented in this study can be used for solution concentrations up to approximately 0.7 mM. The ionic concentration profiles obtained by this approach can be used to test and validate the existing electrosorption models, and pseudo-porous electrodes can be modified to observe the effects of pore size, shape and distribution on electrosorption performance. Furthermore, with proper modifications, the microfabricated structure and experimental set-up can be used for CDI-on-a-chip applications and bio-separation devices.

Keywords Capacitive deionization · Laser-induced fluorescence · Visualization · Electrosorption

1 Introduction

Capacitive deionization (CDI) was first proposed in 1960s as a means of separating the dissolved minerals and salts from water by using an electric field applied by high surface area porous electrodes (Blair John and Murphy George 1960; Johnson and Newman 1971). The practical applications remained limited for years, because the desalination performance is limited by the ionic adsorption capacity of electrodes. However, recent improvements in high surface area porous materials, such as activated carbon (Endo et al. 2001; Huang et al. 2012), carbon cloths (Ahn et al. 2007) and aerogels (Pekala et al. 1998; Biener et al. 2011), carbon nanotubes (CNT) (Wang et al. 2011; Dai et al. 2005) and graphene (Humplik et al. 2011), enabled the CDI technology to be more competitive than ever and revived the interest in this topic.

State-of-the-art CDI systems have various advantages, the first one being high energy efficiency. Since CDI systems have the capability to store the ions through electrostatic forces, analogous to the storage of electric charge in capacitors, it is possible to recover a portion of input energy while cleaning, or regenerating, the electrodes. Secondly, the system performance shows an increase with decreasing inlet stream concentration (Demirer et al. 2013), which means that CDI systems can be cascaded with

Electronic supplementary material The online version of this article (doi:10.1007/s10404-013-1228-3) contains supplementary material, which is available to authorized users.

O. N. Demirer (✉) · C. H. Hidrovo
The University of Texas at Austin, 1 University Station, C2200, Austin, TX 78712, USA
e-mail: od@utexas.edu

C. H. Hidrovo
e-mail: hidrovo@mail.utexas.edu

conventional reverse osmosis (RO) systems to reach higher purity levels than that are achieved by RO only. Thirdly, CDI systems can be designed to be low maintenance, because the porous electrodes are not susceptible to irreversible fouling problems seen in ion-exchange membranes and contamination can be remedied by alkaline or acidic cleaning solutions (Mossad and Zou 2013). Finally, the electrical working principles of CDI dictate that it can treat any ionic pollutant, so it is a versatile method.

The operation of a CDI cell is illustrated in Fig. 1. It can be seen that operation consists of two cycles: (1) desalination, where an external electric potential is applied between electrodes so that the counter ions are electrosorbed onto the porous electrode surface, resulting in decreased outlet concentration, and (2) regeneration, where the two electrodes are electrically shorted or connected to an external load (a capacitor, battery or another CDI cell) so that electrical energy is harvested from the cell as the ions are expelled back into the solution, resulting in a higher outlet concentration. These cycles have to be repeated consecutively, because the surface area and ionic capacity of porous electrodes are limited and electrodes need to be cleaned before they can be reused for ion adsorption.

Various physical and empirical electrosorption models have been developed over the years to understand the underlying physics and to estimate the performance of a CDI system. These include various approaches, such as solving the Nernst–Planck equations to estimate ionic adsorption (Biesheuvel et al. 2011a), using Gouy–Chapman–Stern model to estimate the effect of electrical double layer (EDL) on electrosorption (Biesheuvel et al. 2009), experimentally determining an adsorption velocity for the ions to model the electrosorption (Rios Perez et al. 2013) and using electrical circuit analogies to estimate capacitive behaviour of the system during adsorption and desorption processes (Bazant et al. 2004). However, the basic method to test and verify these results has remained almost the same for four decades and is limited to two types of experimental measurements: (1) Solution concentration is measured at the inlet and outlet of CDI cell to calculate the amount of adsorbed ions, and (2) current passing through the external circuit is measured to calculate the energy input during desalination and energy output during regeneration. Therefore, experimental studies still have to treat CDI systems as "black boxes", and the verification of models has to be performed implicitly, based on the transient behaviour of inlet/outlet concentration and input/output current. Such an approach might be useful to calibrate the models according to various specific CDI systems, but it does not provide any additional insight into the fundamentals of electrosorption process and whether or not the models actually capture the physical phenomena occurring inside the CDI cell correctly. In addition, batch processing CDI systems cannot be monitored by inlet and outlet conductivity probes, since there is no flow of solution during desalination. Finally, the measurements obtained by conventional electrical conductivity probes are only applicable to mixed mean bulk solution concentration, and they cannot be used to obtain concentration profiles within the bulk solution and porous electrodes. The main aim of this paper is to demonstrate a novel experimental set-up and procedure to understand the CDI process by providing a method to obtain actual ionic transport data from within a model CDI cell.

Laser-induced fluorescence (LIF) measurements have been performed in various studies to characterize ion transport in micro- and nano-channels. For example, Kwak et al. (2013) have come up with a microscale electrodialysis set-up and used cationic Rhodamine 6G fluorescent dye as tracer for salt concentration in a NaCl solution to visualize flow vortices and concentration profiles. In addition, Sheridan et al. have introduced a new membraneless deionization method in microchannels, which

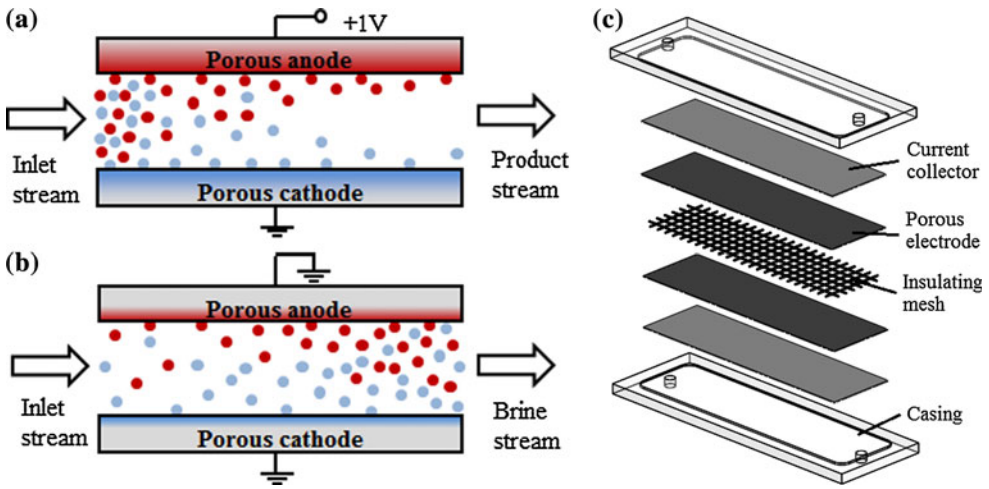

Fig. 1 Overview of CDI operation steps: **a** desalination, **b** regeneration. The colours of porous electrodes represent saturation during desalination and depletion during regeneration. **c** Exploded view of a parallel plate CDI cell

they refer to as bipolar electrode depletion (BED). In this approach, $BODIPY^{2-}$ and Rhodamine B fluorescent dyes were used together to visualize simultaneous electro-osmosis and electromigration effects, and the fluorescent emissions were separated using spectral emission filters (Sheridan et al. 2011). Finally, in the study of Kim et al. (2007), fluorescent nanoparticles were injected into the flow to visualize the vortices around a nanochannel, which acts as a permselective membrane under the application of an external electric field and causes concentration polarization. It can be deduced from these examples that micro- and nano-scale LIF visualization is a feasible way to study ionic transport, but such an approach is yet to be implemented for CDI applications, mainly due to challenges in fabrication of a porous electrode to be used in a microfluidic channel and in obtaining visual access inside the porous electrode.

In this paper, an experimental method is introduced to perform simultaneous in situ concentration measurements of both anions and cations during the CDI process and to visualize ion transport within-pseudo-porous electrodes. Using this method, the effects of CDI cell potential on bulk solution concentration distribution and electromigration of ions within the porous electrodes are studied. This experimental set-up and procedure represents a new visual tool towards understanding the transport phenomena occurring inside a model CDI cell.

2 Experimental set-up

In this section, details of microfluidic device fabrication, dual fluorophore LIF visualization set-up and experimental procedure are provided. Device fabrication is performed in Center for Nano- and Molecular Science, and the experiments are conducted in Multiscale Thermal Fluids Laboratory, at The University of Texas at Austin.

2.1 Microfluidic device fabrication

The top view of the device, presented in Fig. 2b, is representative of the cross-section of a CDI cell presented in Fig. 2a. The device consists of a flow channel of 30 mm length, 0.2 mm width and 0.1 mm depth, with pseudo-porous regions on each side of this channel, acting as porous electrodes. These pseudo-porous electrodes include trenches of 10 μm nominal width and 2 mm length, lying perpendicular to the main flow channel. The electrode regions are fabricated to be highly conductive to mimic the high conductivity porous carbon electrodes widely used in CDI applications. Therefore, once an external electric potential is applied onto the contacts, the whole electrode region becomes charged with minimal resistive loss. In addition, the trenches, or pores, were fabricated not to be straight, but to have roughness elements. This design increases the available adsorption surface area, but also increases the resistance to flow within the pores, which is also the case for porous electrodes used in CDI applications. Therefore, it can be said that the device is a valid representation of a CDI system.

On the other hand, the electrode structure is called "pseudo-porous", due to several reasons. Firstly, both the pore size and electrode size are exaggerated, to be able to observe the flow within the porous structure in more detail and to increase the available adsorption surface area, respectively. Due to large pore size, electrical double layers (EDL) within the pores do not overlap, whereas such an occurrence is possible for mesoporous electrodes. Secondly, the electrode structure of the microfluidic device is much more organized than the structure of a conventional porous electrode, which includes pores of irregular shapes and various sizes. Thirdly, the pores are represented as trenches lying perpendicular to the main channel, separated by solid walls. This means that observing electromigration from one pore to another is impossible and only the electromigration effects along the pore orientation are captured. This issue can be solved by using pillar forests instead of trenches, but electrical contacts to pillars can only be obtained from the bottom, which is a challenging task. These restrictions should be considered when interpreting and comparing the results with other CDI applications.

One of the biggest challenges in designing such a microfluidic device is obtaining a strong electric potential difference between the electrodes on each side of the channel, which necessitates having high conductivity porous regions and an insulating channel base. In the case of an actual CDI system, the electrodes are separated by an insulating mesh, seen in Fig. 1c, to prevent contact and current leakage between two electrodes. On the other hand, in a microfluidic system, the two sides have to be connected by the channel base and they cannot be physically disconnected. One solution to this challenge is to have a highly doped surface region with a junction depth close to channel depth. Provided that the substrate is very lightly doped or intrinsic, this should result in low current leakage through channel base. Another solution to this problem is to use a silicon-on-insulator (SOI) wafer as substrate, which has a buried SiO_2 layer between top (device) and bottom (handle) layers of silicon. This layer provides insulation between the handle layer and conductive device layer. If the device layer is etched all the way down to this intermediate layer, one might physically divide the device layer into two separate sides, which will serve as the anode and cathode sides. The porous electrodes can then be machined into the anode and cathode sides of the device layer. The intermediate oxide

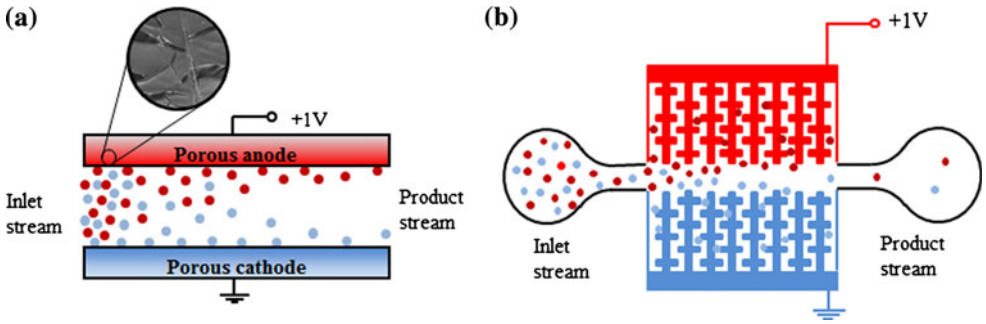

Fig. 2 Schematics of **a** parallel plate CDI cell cross-section and **b** *top view* of the fabricated CDI microstructure (features not to scale). A sample SEM image of the porous electrode is also provided for the case of carbon aerogel

layer also serves as an etch stop during chemical etching of silicon, so that the channel depth can be specified with an uncertainty of 1 μm. The SOI wafers used in this study have a diameter of 76.2 mm, device thickness of 100 μm and resistivity of <0.005 Ω cm, handle thickness of 500 μm and resistivity of >10,000 Ω cm, with a buried SiO_2 layer of 2 μm thickness in between these.

Starting with an SOI wafer, the first step in fabrication process is machining the microchannel and electrodes, and physically separating the device layer into anode and cathode sides. This was performed by contact lithography, using a Suss MA-6 mask aligner, a photomask, shown in Fig. 3a, printed at 25,400 dpi (CAD/Art Services Inc.), SU-8 2025 photoresist and SU-8 Developer (Micro-Chem). The patterned SU-8 was used as a soft mask for Bosch DRIE process performed by Oxford Instruments Plasma Lab 80+ tool. By using alternating C_4F_8 and SF_6 gases in an inductively coupled plasma, the device layer was etched anisotropically down to the buried oxide layer. During this process, C_4F_8 gas was utilized to deposit a passivation layer over the surface to protect sidewalls from etching, while SF_6 gas was used to bombard the wafer surface with ions in the vertical direction (Laermer and Urban 2003). Since the SiO_2 etch selectivity in DRIE is around 120–200:1 (Kovacs et al. 1998), etching was stopped by the intermediate oxide layer and measurements performed by Dektak 6 M Stylus profilometer indicate that the channel depth obtained by this process is 100 ± 1 μm, with near vertical sidewalls and scalloping on the order of 1 μm.

Once the microchannel and porous electrodes were machined, a 76.2-mm-diameter, 500-μm-thick Pyrex wafer was anodically bonded onto the device layer, thus hermetically sealing the channel while providing visual access for visualization from the front side of the microfluidic device. The bonding set-up needed for this process consists of a high-voltage power supply (ThermoEC EC6000-90), a digital hot plate (Thermo Scientific), a $6'' \times 6'' \times 0.5''$ aluminium block as anode, a $6'' \times 6'' \times 2''$ refractory brick for insulation and a stainless steel probe as cathode. Silicon and glass wafers were bonded by following the well-established procedure presented in various publications such as (Albaugh et al. 1988; Lee et al. 2000), and bonding

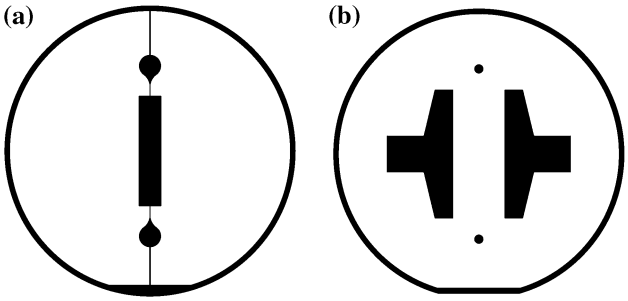

Fig. 3 Photomasks used in the photolithography step: **a** *front side mask* of the channel and porous electrodes (seen as totally *black* due to sub-resolution trench size), **b** *back side mask* of the electrical contacts and inlet/exit ports

was completed in 2 h at 800 V and 400°. It should be noted that Si and Pyrex wafer surface qualities are critical for this step; therefore, bonding was performed right after the fabrication of microchannel, thus decreasing the chance of surface contamination.

The next step in fabrication is machining the fluid inlet and outlet ports, in addition to incorporating the electrical contacts. Both the fluid and electrical access to the device were established by a backside etch through the handle layer. The process for backside etch is similar to the first litho-etch step. The soft mask is patterned by contact lithography, using the photomask in Fig. 3b, and Bosch DRIE is used to etch through the 500-μm-thick handle layer. Performing such a backside etch is possible either by a mask aligner with backside alignment feature or a mask containing alignment marks for the wafer itself. The second option was used for the case of this study, and the SOI wafer was aligned with respect to the mask for both the first and second photolithography steps to assure that the front- and backside features align correctly. This second etch step is also stopped by the oxide layer, at which point a reactive ion etching (RIE) process was used to etch away the SiO_2 layer to reveal the microchannel inlet/outlet ports and expose the device layer for electrical contacts. The gases used to create the plasma for RIE were CF_4 and O_2.

After the back etch was completed, SU-8 photoresist was not removed, but instead it was used as a mask in physical vapour deposition (PVD) process to deposit

aluminium onto device layer at the electrical contact regions. The inlet and outlet ports were also blocked by temperature-resistant Kapton tape to prevent coating and contamination of microchannel. The aluminium pellets (Sigma-Aldrich) were placed inside tungsten boats (Ted Pella, Inc.) and were evaporated by using a Denton Thermal Evaporator, until an aluminium layer of approximately 1 μm was deposited onto the backside of the device. Aluminium deposition is preferred to have a reliable Ohmic contact onto highly p-doped device layer, and it is important that the contact metal is suitable with the type of dopant used in the device layer to prevent having a Schottky contact, which acts as a diode due to the depletion layer at the metal–Si interface.

The final requirement of the microfluidic device is to have a reliable micro–macro-fluid interface. At this point, polydimethylsiloxane (PDMS), a popular material in microfluidics, was chosen as interconnect, due to its flexibility, ease of machining and sealing abilities. Firstly, two PDMS slabs were prepared by regular methods present in the literature (Folch et al. 1999; Fiorini et al. 2003), and holes at the appropriate diameter to have an interference fit with the tubing were punched in these slabs. Then, these two slabs were bonded on the SOI device by the interlayer bonding method presented in (Quaglio et al. 2008), so that the holes correspond to inlet and outlet ports on the device. The interlayer PDMS at sufficient thickness can seal the surface irregularities on the device and provide a reliable fluid interconnect. Finally, the two ends of the microfluidic channel that are left open due to the separation of device layer into two were plugged with PDMS, to avoid any fluid leakage.

The fabrication steps described in this section are summarized in Fig. 4, and a general overview of the final device is provided in Fig. 5.

2.2 LIF microscopy set-up

This set-up aims to visualize simultaneous transport of cations and anions; therefore, a solution containing a cationic dye, Sulforhodamine B (SRB), and an anionic dye, Fluorescein, was used in the experiments. These fluorescent dyes have been characterized and used in various studies (Song et al. 2000; Kim and Yoda 2010; Ray and Nakahara 2001). They can also be sufficiently excited at 514 nm; therefore, only a single illumination source is needed. In addition, their emission and excitation spectra are far enough, so that emission reabsorption problems are minimal and each emission signal can be sufficiently isolated by band-pass filters. Spectral information about these dyes and the optics used in their visualization are provided in Fig. 6.

An epifluorescence microscope (Nikon Eclipse LV100) was paired with a self-contained multi-line argon ion Laser (Edmund Optics) to have a compact and versatile LIF set-up. A dichroic mirror, ZT514rdc (Chroma Technology Corp.), was used to reflect the 514-nm wavelength excitation from the Ar ion laser onto the microfluidic device and transmit the fluorescence emission from the device above 530 nm wavelength. Since the emission from the device includes both SRB and Fluorescein emissions, they have to be spectrally separated to obtain two separate images of the device. This was performed by a DV2 two-channel simultaneous imaging system (Photometrics), which includes a second dichroic mirror, ZT561rdc (Chroma Technology Corp.) and two emission filters, ET537/29 m and HQ620/60 m, to separate and isolate the Fluorescein and Sulforhodamine emissions. These two light beams are then reflected onto the imaging array of a Coolsnap HQ CCD camera (Photometrics). Thus, two separate fluorescence images of the same region on the microfluidic device are recorded by a single CCD array by split-field imaging.

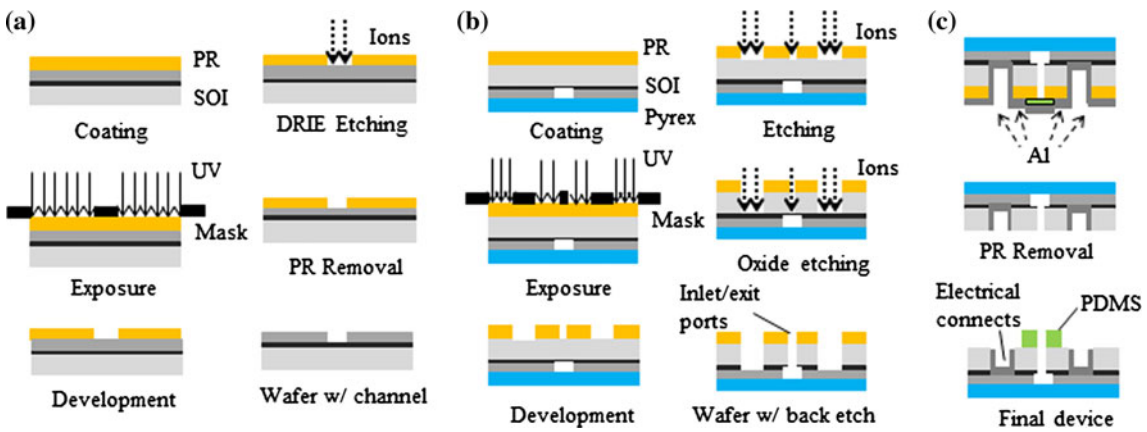

Fig. 4 Fabrication steps from SOI wafer to final device: **a** photolithography and DRIE to fabricate microchannel and pseudo-porous electrodes, **b** backside etching to provide electrical and fluid access **c** PVD for electrical contacts and PDMS bonding for fluid interface

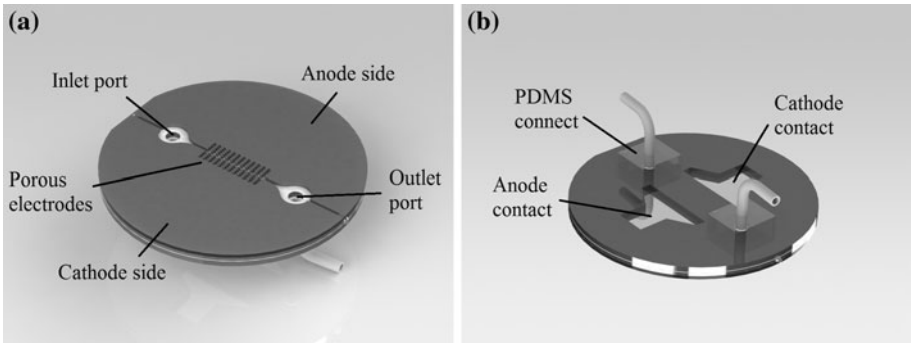

Fig. 5 Overview of final device (features not to scale). **a** Channel and porous electrodes on the *front side*, **b** electrical contacts and fluid connection on the *back side*

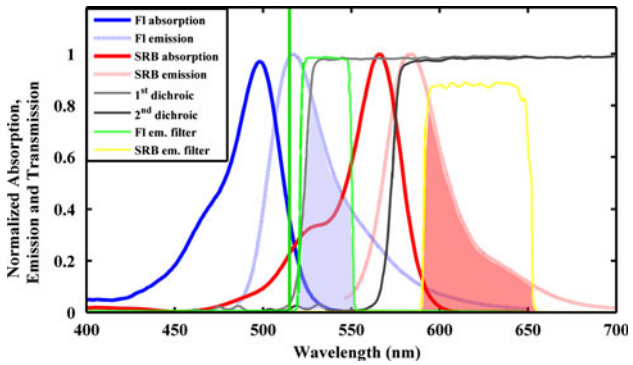

Fig. 6 Spectral properties of fluorophores and optics. *Vertical green line* represents excitation. *Blue* and *red shaded* regions indicate collected emission from Fluorescein and SRB, respectively

To overcome fluid capacitance effects associated with small hydraulic diameters, a pressure-driven system was used to provide flow. Beakers containing solutions were placed inside a pressure chamber machined out of Al, and chamber pressure was controlled via an electronic pressure regulator (Proportion Air) to modulate flow rate, which was measured by a liquid flow sensor (Sensirion AG). The electric power input for the device was supplied by an E3647A power supply (Agilent).

The overview of this experimental set-up is provided in Fig. 7.

2.3 Experimental methods

The microfluidic device, detailed in Sect. 2.1, and the LIF microscopy set-up, detailed in Sect. 2.2, were used in conjunction during the experiments. The microfluidic device was placed on the microscope stage, with front side facing up for visualization. The inlet and outlet fluidic ports on the backside of the device were connected to flow metre outlet tube and a drain tube, respectively. Electrical connection was established by applying highly conductive copper tape on the backside electrical contact regions, soldering the electrical wires onto the copper tape and enabling safe removal and maintenance of electrical contacts without damaging the microfluidic device.

Three types of experiments were performed to prove the functionality of fabricated microfluidic device and LIF visualization set-up: (1) high magnification single fluorophore LIF tests, (2) low magnification single fluorophore LIF tests and (3) dual fluorophore LIF tests. In the first type of experiments, SRB was used to examine the effect of electrical potential on the concentration distribution within the bulk solution. A 20× Plan Fluor objective was used to image the main channel with high spatial resolution. Results from these tests were analysed to verify that the new microfluidic device concept is functional and that the electrical field generated by the device is capable of affecting the bulk solution. In the second type of experiments, SRB was used to study the electromigration of ions from bulk solution into the porous structure by using a 4× Plan Fluor objective and imaging both the bulk solution and the porous electrode. The bulk solution concentration decrease due to ionic adsorption onto the porous electrode was also examined. The results from these tests are indicative of the ionic capacity of porous electrodes and overall desalination performance. Third type of experiments was performed by using a mixture of SRB and Fluorescein dyes, to observe the simultaneous behaviour of cations and anions during desalination. Both electrodes and the bulk solution were imaged to observe coion expulsion and counter ion adsorption within the electrodes and resulting concentration profiles within the bulk solution.

In all tests, the microchannel was first filled with dye solution, and then flow was stopped before applying the electric field, which resembles batch processing with intermittent flow. Therefore, diffusion and electromigration effects were analysed independent of advection. In addition, the model CDI cell was "flushed" with high flow rate solution after each desalination test for several minutes while electrically shorting the electrode regions for regeneration. The CDI cell potential was ranged from 1.5 to 3.0 V, where the onset of electrolysis is experienced. This points to electrical transmission losses of approximately 50 %.

CDI systems are limited by ionic adsorption capacity of the porous electrodes. Due to this ionic capacity limit,

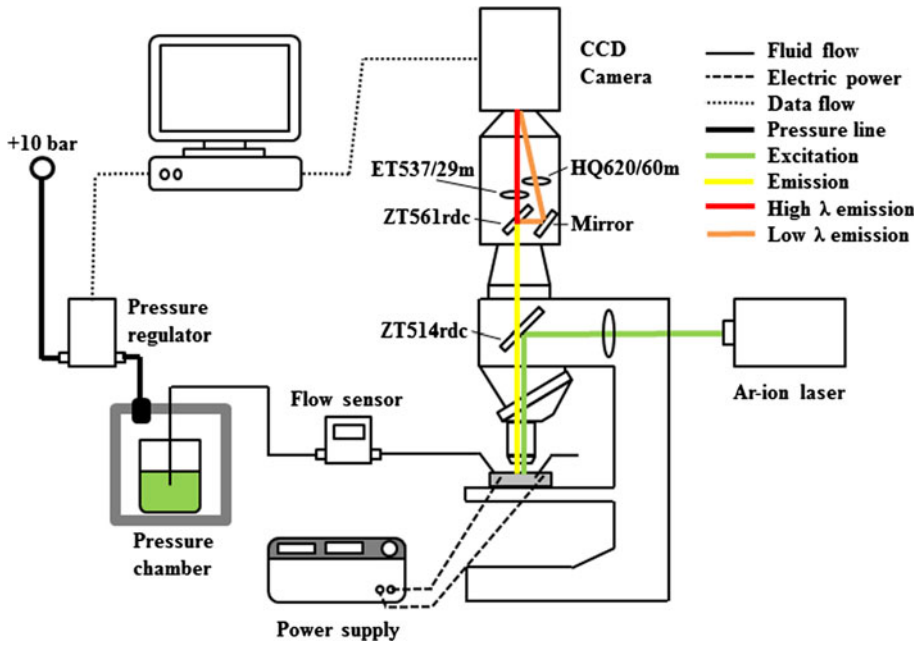

Fig. 7 Overview of the experimental set-up

concentration changes due to capacitive deionization are more significant at lower solution concentrations. For this reason, concentrations of Fluorescein and SRB solutions prepared in this study are relatively low. For the first type of tests, 1.5 μM SRB solutions were used, for the second type of tests, 3.0 μM solutions were used to compensate for low NA 4× objective, and for the third type of test, 1.5 μM Fluorescein and 0.75 μM SRB solutions were used to have balanced intensity values on both DV-2 channels. Such low fluorophore concentrations mean low optical depth, in which case self-quenching effects are negligible and emission intensity can be linearly related to local concentration (Carroll and Hidrovo 2012). To verify this assumption, SRB solutions with various concentrations were prepared and imaged within the microfluidic device. The resultant emission versus concentration behaviour is provided in Fig. 8. As seen in this figure, the linear least squares regression fit lies within the uncertainty bounds of the concentration measurements for concentrations up to 130 μM. Therefore, it can be said that concentration and emission intensity are related linearly. This linearity implies negligible self-quenching effects, so SRB solutions with concentrations up to 130 μM are defined to have low optical depth in the case of this study. Since the low optical depth conditions are met in all of the experiments, "intensity" and "concentration" can be used interchangeably and the calibration equation is given as:

$$I = a \times C + b \tag{1}$$

where I denotes normalized intensity, C denotes measured concentration, and calibration constants a and b are found as $(3.59 \pm 0.08) \times 10^{-3}$ and $(94.1 \pm 3.8) \times 10^{-3}$, respectively.

For concentrations higher than 130 μM, self-quenching effect starts to become pronounced and the slope of emission versus concentration curve decreases. Therefore, emission versus concentration relationship is not linear anymore, and this has to be taken into account during calibration process. If the concentration is increased higher than 700 μM, it is seen that the self-quenching effect becomes even more pronounced and increased concentration reduces emission intensity. Due to this self-quenching effect, the upper bound of the concentrations that can be measured by the method presented in this study is approximately 700 μM, provided that nonlinear emission/concentration behaviour is accurately captured.

The main challenge in using low-concentration fluorescent dye solutions is the weak emission intensity. Since there is always random noise captured by the imaging system, it is important to have significant emission

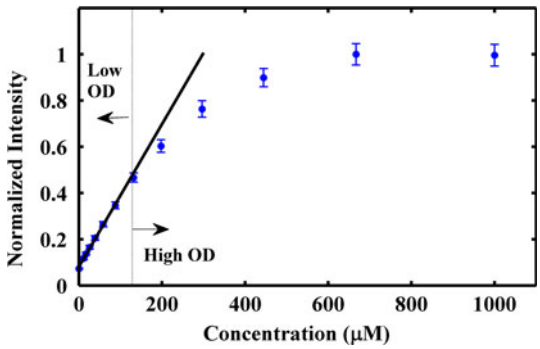

Fig. 8 Calibration curve for emission intensity as a function of solution concentration. *Dots* indicate measurement points, and *solid line* represents linear least squares regression fit for low optical depth (OD) region

intensity from the channel to be visualized, so that signal-to-noise ratio can be kept as high as possible. Considering that the electromigration and diffusion processes are relatively slow, low emission intensities associated with dilute solutions can be remedied by higher exposure time, the duration for which the micropixel array of the CCD camera is exposed to light. This approach increases the captured emission intensity, but, although to a lesser extent, it also increases the noise captured from the environment. In addition, longer exposure times mean lower frame rate and lower temporal resolution, since the system is not capable of sensing the changes occurring in less time than the exposure duration. Therefore, there exists a captured intensity versus noise and temporal resolution trade-off in the determination of the optimal exposure time. For the case of this study, exposure time of the images taken with 10× and 20× objectives was chosen as 1 s and exposure time of the images taken with 4× objective was chosen as 2 s. This adjustment in exposure time is necessary to compensate for the lower numerical aperture (NA) of 4× lens, which results in lower fluorescence emission intensity. The noise problem associated with the increased exposure time for low magnification experiments is solved by using data processing techniques, which are detailed in Sect. 2.4.

All solutions used in this study were prepared by using deionized water as the solvent, because the ions released by buffer solutions contribute to deionization process and interfere with the measurements. Therefore, pH levels cannot be strictly controlled and one should either check the solution pH levels regularly or use fluorophores with good emission stability at a wide pH range to have reliable concentration measurements. Out of these two dyes, Sulforhodamine exhibits pH-independent fluorescence emission between 4 and 9, whereas Fluorescein exhibits pH-dependent emission. Therefore, single fluorophore tests were performed by SRB and the pH of dual fluorophore mixtures were regularly monitored to overcome emission instability.

2.4 Data processing

Fluorescent radiation emitted by the dyes inside the microfluidic device was recorded into TIF stacks. These TIF files were then imported into MATLAB to perform image processing. Firstly, background noise, which was measured for an area on the device with no fluorophores, was subtracted from the images. By the removal of background noise, it was assured that all the measured intensity is due to the fluorescent emission. Then, the intensity at every pixel was normalized by the intensity value measured for a uniform concentration dye solution to compensate for the nonuniformity of laser excitation and aberrations in the optical elements. By normalizing the intensities at every pixel, it was assured that the gradients in the measured intensity were not due to the optical system used during the experiments, but due to concentration gradients within the microfluidic device. Such an intensity normalization procedure is not needed if ratiometric techniques are used, so that the ratio of fluorescent intensities of two dyes is considered instead of individual intensities. However, in the case of this study, independent concentration profiles of two different dyes should be known to be able to visualize simultaneous electromigration of oppositely charged particles, so this second data processing step is necessary.

Since the fluorescent dyes have a wide range of emission spectra, it is not practically possible to completely separate the two emissions without using very narrow emission filters, which decrease the emission intensity drastically. This problem is also illustrated in Fig. 6, where the emissions of two dyes overlap within the filtered ranges. To overcome this, the amount of cross-talk between SRB and Fluorescein channels should be characterized, which was performed by imaging two adjacent microfluidic channels, one filled with SRB and another filled with Fluorescein, within the same frame. Average fluorescence intensity that passes on to the other channel was found to be 8.2 % for SRB and 10.3 % for Fluorescein. Using these two values and the measured intensity profiles, actual concentrations of both dyes were calculated by solving the following 2-by-2 linear system of equations for all the pixels:

$$\begin{bmatrix} 1 & 0.103 \\ 0.082 & 1 \end{bmatrix} \begin{bmatrix} I_{SrB} \\ I_{Fl} \end{bmatrix} = \begin{bmatrix} I_1 \\ I_2 \end{bmatrix} \quad (2)$$

where I indicates intensity, subscripts SrB and Fl stand for SRB and Fluorescein, and subscripts 1 and 2 indicate the DV-2 channel number. In this configuration, channels 1 and 2 are used to measure the fluorescence intensity of SRB and Fluorescein, respectively.

One specific challenge in extracting the concentration from fluorescence intensity measurements is seen in the data processing of desalination tests performed with 4× objective lens. It has been mentioned in the previous section that the captured fluorescence intensity decreases with decreasing NA and higher exposure time was necessary to overcome this problem. However, increasing the exposure time also increases the background noise. In addition to this noise, the area imaged with the 4× lens is relatively large and spatial resolution within the porous structure is considerably less than high magnification lenses, so it is impossible to draw a straight line through the porous structure and record the concentration along that cross-section. Therefore, for low magnification tests, the concentration profiles for 25 separate pores were averaged and a smoothing curve fit was applied to the average

concentration profile to overcome noise problems. Such a curve fit process is exemplified in Fig. 9.

As seen in Fig. 9, the concentration profile contains random noise. The error due to this noise is characterized by finding the root mean square deviation (RMSD) between the smoothing fit and actual data points and normalizing the RMSD by the range of measured intensities to obtain the normalized RMSD (NRMSD), given by Eq. 3:

$$\mathrm{NRMSD} = \frac{\sqrt{\frac{1}{N}\sum_{i=1}^{N}(I_i - \hat{I}_i)^2}}{I_{\max} - I_{\min}} \tag{3}$$

where N indicates the total number of data points, I indicates measured intensity, $\hat{I}$ indicates smoothing fit intensity, and subscripts *max* and *min* indicate the maximum and minimum values in the data set. The NRMSD values obtained by this method are included with the concentration profiles presented in Sect. 3.2.

3 Results

The results from all three types of LIF experiments are presented, and discussion of the underlying phenomena is provided in this section.

3.1 Single fluorophore LIF: effects of electric field on bulk solution concentration

Single fluorophore LIF experiments were first used to observe the effect of electric field applied by the porous electrode on the bulk solution concentration. This effect has been previously modelled for "symmetric binary electrolytes with equal anion and cation mobilities" (Bazant et al. 2004). However, unlike the findings of this study, which estimate the bulk concentration to decrease symmetrically across the channel, application of the electric field shifted the SRB concentration peak towards the cathode, resulting in an asymmetric concentration profile across the channel, as seen in Fig. 10a. There are several reasons for such a difference in results. Firstly, the SRB ions are significantly larger than the counter ions they release upon dissolution in water; therefore, the symmetric electrolyte assumption does not hold. Secondly, the electrodes in this experimental set-up are more complex than the simple case of parallel flat electrodes. Thirdly, and more importantly, the flow of ions into the porous structure is impeded by the presence of the porous structure itself. This physical resistance of porous structure against electromigration can be reduced by having higher porosity electrodes, but it is always present to some degree. This effect has already been taken into account four decades ago (Johnson and Newman 1971) by defining an "electrode ionic resistance" in an electrical circuit analogy and more recently (Biesheuvel et al. 2011a) by defining an "effective diffusion coefficient" of ions within the electrode, which is lower than the diffusion coefficient in the bulk solution. Due to this known effect, the flux of ions from electrode/bulk solution interface towards the porous electrode is less than the flux of ions from bulk solution to electrode/bulk solution interface. Thus, the cations are accumulated at the cathode/bulk solution interface, and for the same reason, they are depleted from anode/bulk solution interface. This results in the asymmetric concentration profile across the bulk solution, seen in Fig. 10a.

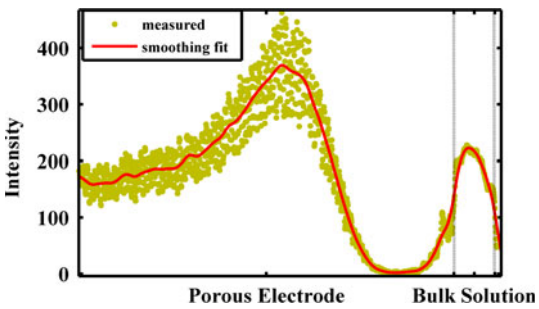

Fig. 9 Sample smoothing fit performed for desalination tests with 4× objective. Measurement points inside the porous structure represent average intensity of 25 pores at that location

For a better understanding of the processes occurring during desalination, the temporal variation of the concentration profile across the channel has been provided in Fig. 10b. As seen in this figure, the concentration across the channel is symmetric at the beginning of desalination ($t = 3$ s), and the concentration gradients on both sides of the channel indicate that SRB ions are diffusing into the anode and cathode. As the electric field is applied, it is seen that the bulk concentration increases, more significantly on the anode side ($t = 8$ s). This is due to the fact that application of the electric field repels the SRB ions from within the porous anode. Membrane CDI (MCDI) processes have been specifically developed to overcome this coion expulsion effect and to increase adsorption efficiency (Kim and Choi 2010; Biesheuvel et al. 2011b). After this initial increase, it is seen that the SRB concentration peak shifts towards the cathode, indicating electromigration of ions within the bulk solution ($t = 10$ s, 16 s). This is followed by the electromigration of ions from the bulk solution to the pores of the anode, which results in decrease in overall bulk concentration ($t = 26$ s). It is observed that after this initial transient period, the shape of bulk concentration profile does not change significantly, but the values decrease with time due to electrosorption inside the porous electrodes, until the whole electrode is saturated by adsorbed ions and the electric field is completely shielded by the electrical double layer (EDL).

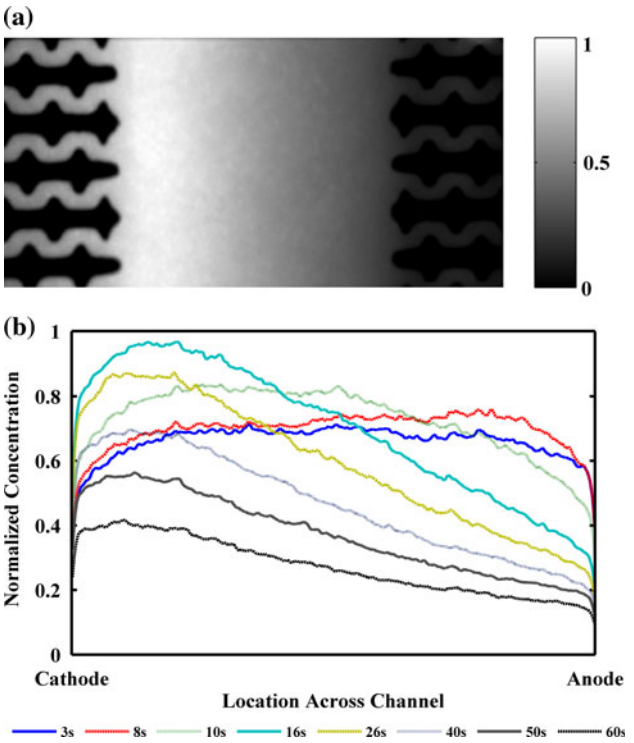

Fig. 10 **a** Asymmetric bulk concentration distribution influenced by electrical field, showing the accumulation of cations at the cathode/bulk solution interface and the depletion of cations from the anode. **b** Time-dependent concentration profiles within the bulk solution for SRB. The concentration distribution within porous structure is omitted

After seeing that CDI cell potential affected the bulk concentration distribution significantly, tests were run at various CDI cell potentials to characterize this effect. In Fig. 11a, time-dependent average bulk concentrations are shown for desalination tests performed at 1.8, 2.2 and 2.6 V. The coion expulsion effect is seen as an initial increase in bulk solution concentrations in the first 10 s for all three tests. In addition, it is seen that the coion expulsion and counterion adsorption rates are almost the same between 30 and 60 s for desalination test with 2.2 V applied voltage, resulting in an almost constant bulk solution concentration during this period. After 60 s, the coions in the anode are almost depleted and the concentration decrease is driven by counterion adsorption into the cathode. The important difference between these three tests is the rate of concentration decrease, or the rate of ionic adsorption, after this initial period, which is found as 0.008, 0.088 and 0.212 μM/s for 1.8, 2.2 and 2.6 V, respectively. An "adsorption velocity" term to model this initial adsorption rate has been used previously by (Rios Perez et al. 2013), and it was assumed that this adsorption rate would decrease linearly with increasing electrode concentration, due to saturation and EDL shielding effects. In this study, it is shown that the electrosorption rate is also strongly dependent on the CDI cell potential. To observe the effect of CDI cell potential, and thus the adsorption rate, on bulk solution concentration, normalized concentration profiles obtained after the initial coion expulsion period are also illustrated in Fig. 11b for desalination at 1.8, 2.2 and 2.6 V CDI cell potentials. The concentration profiles provided in Fig. 11b indicate that the asymmetry and the shift of peak in bulk solution concentration are directly related to CDI cell potential and thus the electrosorption rate. These results are intuitive, since the concentration accumulation at the cathode/bulk solution interface is expected to be more pronounced at high ionic flux conditions.

A sample desalination/regeneration test at 2.6-V CDI cell potential is provided in supplemental video 1. Initial coion expulsion, shift of concentration peak towards the cathode and decrease in the overall bulk solution concentration can all be seen in this video. To assure that bulk solution concentration decrease was not due to photobleaching, deterioration of fluorophores after extended excitation, desalination was stopped after 65 s (around 13 s in supplemental video 1). It was seen that as soon as desalination stopped, the bulk solution concentration increased back to approximately the same level before desalination.

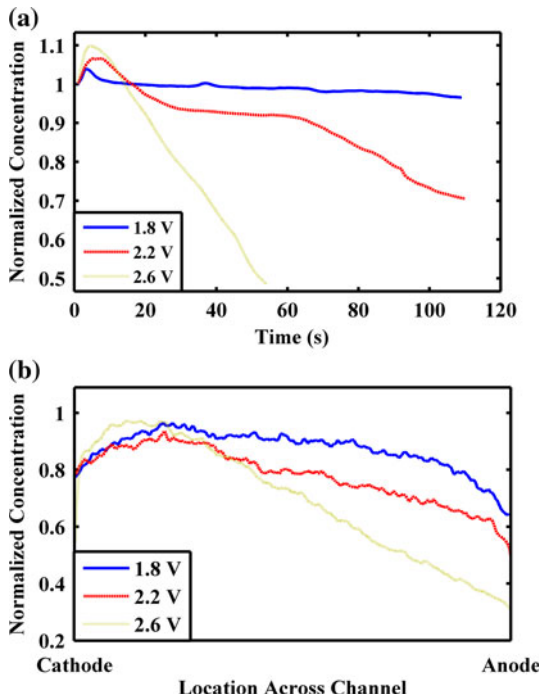

Fig. 11 **a** Bulk SRB concentration for desalination tests at different CDI cell potentials. Coion expulsion seen in the first 15 s and rate of concentration decrease is directly related to CDI cell potential. **b** Concentration profiles during desalination tests performed at different CDI cell potentials. It is seen that the shift of concentration peak and the asymmetry in concentration profile is directly related to CDI cell potential

Therefore, it was verified that the bulk concentration decrease is indeed due to electromigration of SRB ions into the porous electrode.

3.2 Single fluorophore LIF: migration of ions within porous electrodes

Second type of single fluorophore LIF experiments was performed to observe the migration of ions within porous electrodes and the average bulk concentration decrease due to electrosorption. Two sample 2D concentration distributions obtained before and during desalination experiments are illustrated in Fig. 12a, b for SRB. In Fig. 12a, it is seen that SRB has diffused into the porous electrodes at the beginning of desalination experiments, but the bulk concentration is still higher than electrode concentration. The electrode and bulk concentration should equalize provided that enough time is provided for diffusion, but the large width of the porous structure and low bulk solution concentration means very large diffusive time constants. Therefore, experiments are started after 10 min of stabilization. In Fig. 12b, it is seen that concentration within the porous electrodes have increased and the average bulk solution concentration has decreased due to adsorption of ions within the porous electrodes. In addition, the ions within the porous structure have a nonuniform distribution, with higher concentration deeper into the electrode and lower concentration close to the electrode/bulk solution interface.

The transient behaviour of SRB concentration profile within the bulk solution and within the porous electrode during desalination is provided in Fig. 13a, together with the NRMSD associated with each concentration profile. It is seen that the concentration profiles at different instants during desalination process can be captured with less than 10.4 % NRMSD, using the data processing method detailed in Sect. 2.4. As the electric potential is applied, ions inside the porous electrode start migrating deeper into the porous electrode, leaving a region of low concentration behind them, close to the electrode/bulk solution interface. This depletion region drives the ions from the bulk solution into the electrode by concentration diffusion. In time, the ions adsorbed from the bulk solution cause an increase in average electrode concentration and cause the depletion layer to get smaller ($t = 60$–240 s). In Fig. 13a ($t = 240$ s), it is seen that the depletion region still exists, while the bulk concentration is almost zero, meaning that the electrode is not saturated and has the capacity to adsorb more ions. When the electrode is fully saturated, it is expected that concentration in the depletion region is almost the same as bulk concentration, so the ion flux from the bulk solution towards the electrode is zero. Such a depletion effect at the electrode/bulk solution interface has been postulated in the work of (Bazant et al. 2004) and has been used by (Rios Perez et al. 2013) to model the adsorption flux. The existence of a depletion region is verified by the actual concentration profiles obtained in this study, but it was seen that it actually occurred inside the porous electrode. Imaging of the porous electrode close to the electrode/bulk solution interface is also performed by a 10× objective and presented in supplemental video 2 to show the formation of depletion region in more detail.

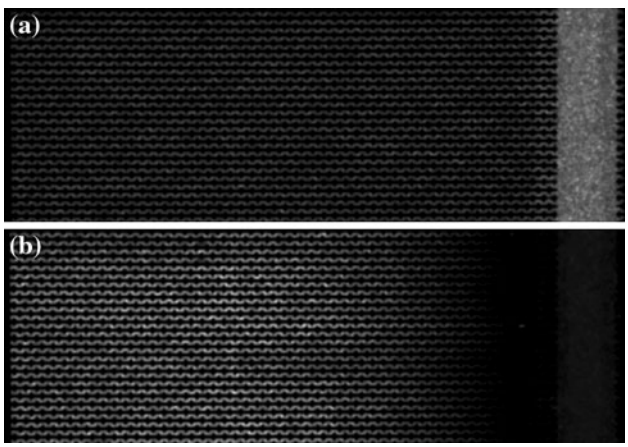

Fig. 12 2D concentration profiles for SRB before (**a**) and during (**b**) desalination. Concentration within the electrode rises with ionic adsorption, whereas bulk concentration decreases. The lowest concentration is seen in the depletion region

In addition to investigating the concentration profiles, the total amount of ions within the solution and the porous electrode are also calculated and presented in Fig. 13b. It is also seen from this figure that the amount of ions in the bulk solution does not decrease in the first 10 s despite the adsorption inside the porous electrode, illustrating the effect of coion expulsion from the anode. After this initial period, the number of ions in the bulk solution decays while the amount of ions in the porous electrode increases. After 200 s, it is seen that the amount of ions within the bulk solution is approximately zero, and the amount of ions within the porous electrode is almost steady at its maximum. It should be noted that the increase in the amount of ions within the cathode is more than the decrease in ions within the bulk solution. This is due to the fact that there are SRB ions within the anode at the beginning of desalination and these ions are also adsorbed within the pores of the cathode. If the ions are distributed evenly between anode and cathode at the beginning of desalination, the amount of ions within the cathode at the end of desalination is expected to be twice the initial amount in the cathode plus the initial amount of ions within the bulk solution. It is seen that the measured change in the amount of ions is 8.2 % less than this expected change, which indicates that the initial distribution of ions was not perfectly

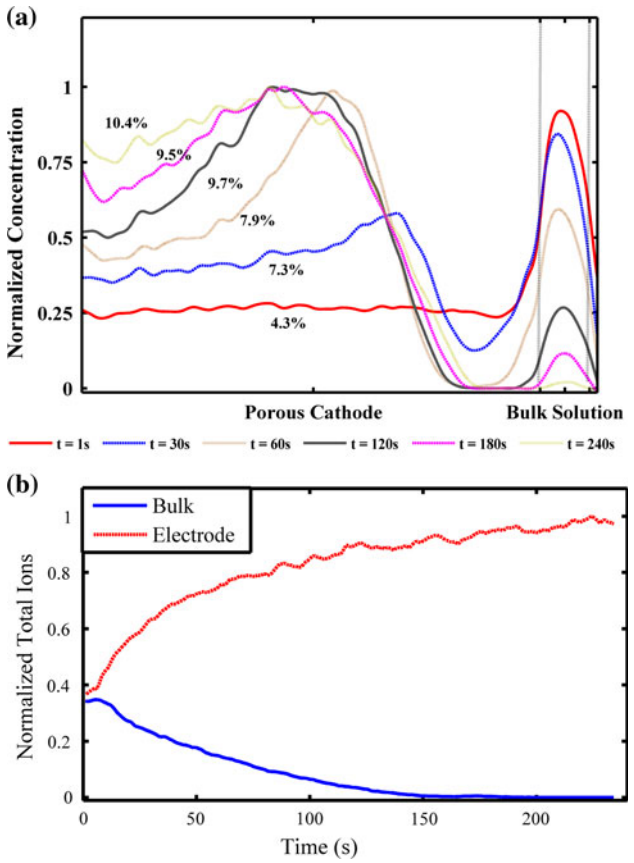

Fig. 13 **a** Time-dependent concentration distribution within the porous electrode and the bulk solution. Formation of depletion region ($t = 30$–60 s), decrease in bulk solution concentration and increase in electrode concentration can be seen. NRMSD values are provided with each concentration profile. **b** Total amount of ions stored in the bulk solution and within the porous electrode a function of time during desalination

homogeneous. This might be the case due to imperfect regeneration of porous electrodes and remnant ions from a previous test.

3.3 Dual fluorophore LIF

Dual fluorophore LIF experiments were performed to observe simultaneous ionic migration of two oppositely charged species within the bulk solution and within the porous electrodes. A sample concentration profile observed 150 s after the application of electric field is provided in Fig. 14a, and the asymmetric concentration profile observed in previous LIF experiments can also be seen in Fig. 14b, which depicts the concentration along a straight line drawn through the middle of a single pore. The distribution of concentrations within porous electrodes indicates that coions that are present within the electrodes before desalination process are repelled by the application of the electric field and counterions are adsorbed within the porous electrodes. It is seen that the bulk concentration change of Fluorescein is significantly more than that of SRB. This is expected to be due to the effects of molecular size and mobility, which favour the electromigration of Fluorescein ($C_{20}H_{12}O_5$) over SRB ($C_{27}H_{30}N_2O_7S_2$). This expectation is supported by the findings of (Werner et al. 2009) and (Milanova et al. 2011), which indicate an order of magnitude difference between the diffusion coefficients of Fluorescein (9.3×10^{-10} m^2/s) and SRB (0.7×10^{-10} m^2/s). It is also thought that the counterions released by Fluorescein upon dissolving in water impede SRB adsorption more, because of the higher Fluorescein concentration. This is observed as a weak depletion region, and thus smaller adsorption flux, for SRB and a strong one for Fluorescein.

A time lapse of the first 150 s of desalination cycle is provided in Fig. 15. It is seen that both dyes have diffused into both electrodes by diffusion at the beginning of desalination ($t = 3$ s). As the electric potential is applied, both SRB and Fluorescein are expelled from anode and cathode, respectively. However, the electromigration of Fluorescein from the bulk solution into the anode is significantly faster

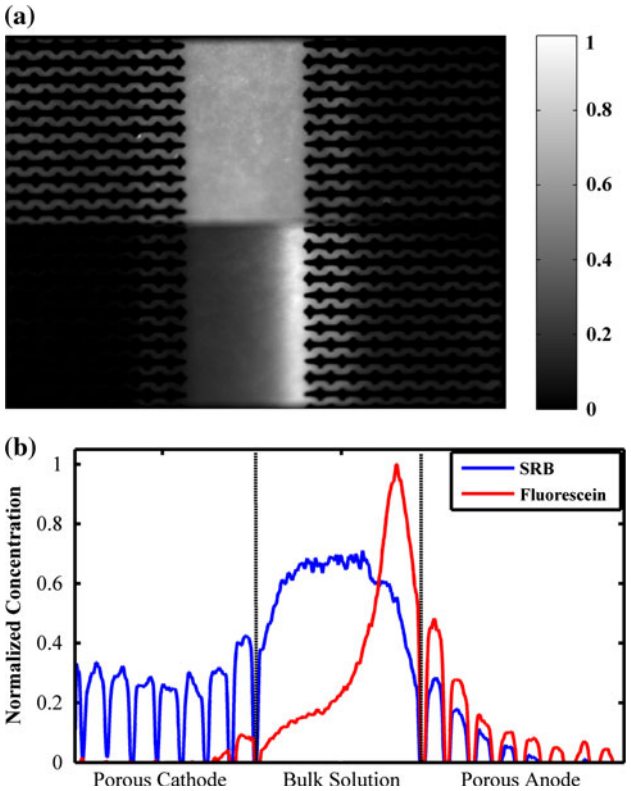

Fig. 14 **a** Snapshot of the model CDI cell 150 s after beginning of desalination. SRB (*top*) and Fluorescein (*bottom*) concentrations. **b** Concentration profile across the channel section in Fig. 14a. SRB is depleted in anode and concentrated within cathode, with almost uniform bulk concentration. Fluorescein is depleted in the cathode and concentrated within the anode, with most of the Fluorescein concentrated at anode/bulk solution interface

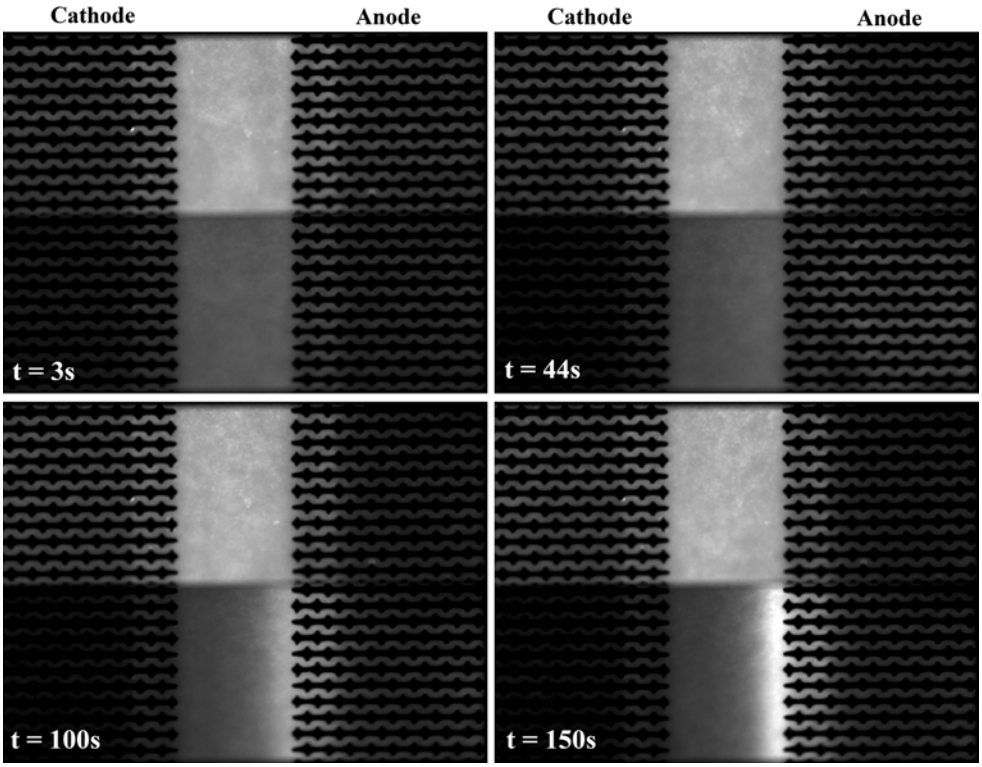

Fig. 15 Time lapse of desalination (0–150 s). ($t = 3$ s) Almost uniform concentration distribution at the beginning of desalination ($t = 44$ s). Coions are expelled from both electrodes, and Fluorescein concentration in anode increases significantly ($t = 100$ s). Fluorescein ions migrate further into the electrode to form a depletion region ($t = 150$ s). Bulk SRB concentration has not changed noticeably, whereas bulk Fluorescein concentration has shifted towards the anode

than electromigration of SRB in the opposite direction ($t = 44$ s). At 100 s, it is seen that the highly concentrated Fluorescein ions within anode have started to migrate deeper into the porous electrode, creating a stronger depletion region, whereas the depletion region in Sulforhodamine is much weaker. This effect is also observed in bulk solution concentration distributions. It is seen that Fluorescein ions within the bulk start to build up at the anode/bulk solution interface, whereas SRB ions are more uniformly distributed among bulk solution. After 150 s of desalination, it is seen that Fluorescein ions have been significantly concentrated at the anode/bulk solution interface with a strong depletion layer inside the electrode, indicating high adsorption flux into the electrode. After this point, the shape of either concentration profile does not change noticeably, but the average concentrations decrease due to electromigration into porous electrodes. This behaviour observed during desalination experiments underscores the selectivity of CDI towards higher mobility ions.

4 Conclusions

In this study, a novel microfluidic device was fabricated to be used in study of ionic transport in capacitive deionization process. The fabricated device features flow channels, pseudo-porous electrodes and electrical contacts integrated on a silicon-on-insulator chip. The simultaneous transport of anions and cations within this device is visualized by laser-induced fluorescence, using cationic SRB and anionic Fluorescein dyes. The fluorescence emission from these dyes was spectrally separated and used for tracing the two oppositely charged particles independently. Single and dual fluorophore desalination tests were run to prove that the concept works. Effects of electrical field on bulk solution concentration profile and electromigration of ions within porous electrodes were studied by single fluorophore LIF experiments. Transient concentration profiles were obtained within the porous electrodes, and the effect of CDI cell potential on electrosorption rate is quantified. Simultaneous concentration measurements for both anions and cations were also performed by dual fluorophore LIF tests, and the effects of ion mobility on transport were illustrated. It was seen that fluorophores with similar size and mobility should be chosen in order to observe comparable electrosorption of both anions and cations. This study serves to be the first in providing visual access into the CDI process. Future work will be focused on fabrication of higher capacity porous electrodes to represent the actual porous electrode

structures more accurately and to come up with a CDI-on-a-chip application.

Acknowledgments The authors would like to thank Dr. Myeongsub Kim and Dr. Tae Jin Kim for their help in LIF visualization and microscopy set-up. This research was funded by The University of Texas start-up funds and The University of Texas System STARS.

References

Ahn H-J, Lee J-H, Jeong Y, Lee J-H, Chi C-S, Oh H-J (2007) Nanostructured carbon cloth electrode for desalination from aqueous solutions. Mater Sci Eng A 449–451:841–845. doi:10.1016/j.msea.2006.02.448

Albaugh KB, Cade PE, Rasmussen DH (1988) Mechanisms of anodic bonding of silicon to Pyrex glass. In: Solid-state sensor and actuator workshop, 1988. Technical Digest., IEEE, 6–9 Jun 1988, pp 109–110. doi:10.1109/SOLSEN.1988.26450

Bazant MZ, Thornton K, Ajdari A (2004) Diffuse-charge dynamics in electrochemical systems. Phys Rev E 70(2):021506

Biener J, Stadermann M, Suss M, Worsley MA, Biener MM, Rose KA, Baumann TF (2011) Advanced carbon aerogels for energy applications. Energy Environ Sci 4(3):656–667

Biesheuvel PM, van Limpt B, van der Wal A (2009) Dynamic adsorption/desorption process model for capacitive deionization. J Phys Chem C 113(14):5636–5640. doi:10.1021/jp809644s

Biesheuvel PM, Fu Y, Bazant MZ (2011a) Diffuse charge and Faradaic reactions in porous electrodes. Phys Rev E 83(6):061507

Biesheuvel PM, Zhao R, Porada S, van der Wal A (2011b) Theory of membrane capacitive deionization including the effect of the electrode pore space. J Colloid Interface Sci 360(1):239–248

Blair John W, Murphy George W (1960) Electrochemical demineralization of water with porous electrodes of large surface area. In: SALINE WATER CONVERSION, vol 27. Advances in Chemistry, vol 27. American Chemical Society, pp 206–223. doi:10.1021/ba-1960-0027.ch020

Carroll B, Hidrovo C (2012) Experimental investigation of inertial mixing in colliding droplets. Heat Transf Eng 34(2–3):120–130. doi:10.1080/01457632.2013.703087

Dai K, Shi L, Fang J, Zhang D, Yu B (2005) NaCl adsorption in multi-walled carbon nanotubes. Mater Lett 59(16):1989–1992

Demirer ON, Naylor RM, Rios Perez CA, Wilkes E, Hidrovo C (2013) Energetic performance optimization of a capacitive deionization system operating with transient cycles and brackish water. Desalination 314:130–138. doi:10.1016/j.desal.2013.01.014

Endo M, Maeda T, Takeda T, Kim YJ, Koshiba K, Hara H, Dresselhaus MS (2001) Capacitance and pore-size distribution in aqueous and nonaqueous electrolytes using various activated carbon electrodes. J Electrochem Soc 148(8):A910–A914. doi:10.1149/1.1382589

Fiorini GS, Jeffries GD, Lim DS, Kuyper CL, Chiu DT (2003) Fabrication of thermoset polyester microfluidic devices and embossing masters using rapid prototyped polydimethylsiloxane molds. Lab Chip 3(3):158–163

Folch A, Ayon A, Hurtado O, Schmidt MA, Toner M (1999) Molding of deep polydimethylsiloxane microstructures for microfluidics and biological applications. J Biomech Eng 121(1):28–34

Huang Z-H, Wang M, Wang L, Kang F (2012) Relation between the charge efficiency of activated carbon fiber and its desalination performance. Langmuir 28(11):5079–5084. doi:10.1021/la204690s

Humplik T, Lee J, O'Hern SC, Fellman BA, Baig MA, Hassan SF, Atieh MA, Rahman F, Laoui T, Karnik R, Wang EN (2011) Nanostructured materials for water desalination. Nanotechnology 22(29):292001

Johnson AM, Newman J (1971) Desalting by means of porous carbon electrodes. J Electrochem Soc 118(3):510–517

Kim Y-J, Choi J-H (2010) Enhanced desalination efficiency in capacitive deionization with an ion-selective membrane. Sep Purif Technol 71(1):70–75

Kim M, Yoda M (2010) Dual-tracer fluorescence thermometry measurements in a heated channel. Exp Fluids 49(1):257–266. doi:10.1007/s00348-010-0853-9

Kim SJ, Wang Y-C, Lee JH, Jang H, Han J (2007) Concentration polarization and nonlinear electrokinetic flow near a nanofluidic channel. Phys Rev Lett 99(4):044501

Kovacs GTA, Maluf NI, Petersen KE (1998) Bulk micromachining of silicon. Proc IEEE 86(8):1536–1551. doi:10.1109/5.704259

Kwak R, Guan G, Peng WK, Han J (2013) Microscale electrodialysis: concentration profiling and vortex visualization. Desalination 308:138–146. doi:10.1016/j.desal.2012.07.017

Laermer F, Urban A (2003) Challenges, developments and applications of silicon deep reactive ion etching. Microelectron Eng 67–68:349–355. doi:10.1016/S0167-9317(03)00089-3

Lee TMH, Lee DHY, Liaw CYN, Lao AIK, Hsing IM (2000) Detailed characterization of anodic bonding process between glass and thin-film coated silicon substrates. Sens Actuators A 86(1–2):103–107. doi:10.1016/S0924-4247(00)00418-0

Milanova D, Chambers RD, Bahga SS, Santiago JG (2011) Electrophoretic mobility measurements of fluorescent dyes using on-chip capillary electrophoresis. Electrophoresis 32(22):3286–3294. doi:10.1002/elps.201100210

Mossad M, Zou L (2013) Study of fouling and scaling in capacitive deionisation by using dissolved organic and inorganic salts. J Hazard Mater 244–245:387–393. doi:10.1016/j.jhazmat.2012.11.062

Pekala RW, Farmer JC, Alviso CT, Tran TD, Mayer ST, Miller JM, Dunn B (1998) Carbon aerogels for electrochemical applications. J Non-Cryst Solids 225:74–80. doi:10.1016/s0022-3093(98)00011-8

Quaglio M, Canavese G, Giuri E, Marasso S, Perrone D, Cocuzza M, Pirri C (2008) Evaluation of different PDMS interconnection solutions for silicon, Pyrex and COC microfluidic chips. J Micromech Microeng 18(5):055012

Ray K, Nakahara H (2001) Adsorption of sulforhodamine dyes in cationic Langmuir–Blodgett films: spectroscopic and structural studies. J Phys Chem B 106(1):92–100. doi:10.1021/jp011946d

Rios Perez CA, Demirer ON, Clifton RL, Naylor R, Hidrovo C (2013) Macro analysis of the electro adsorption process in low concentration NaCl solutions for water desalination applications. J Electrochem Soc 160(3):E13–E21

Sheridan E, Knust KN, Crooks RM (2011) Bipolar electrode depletion: membraneless filtration of charged species using an electrogenerated electric field gradient. Analyst 136(20):4134–4137

Song A, Zhang J, Zhang M, Shen T, Tang Ja (2000) Spectral properties and structure of fluorescein and its alkyl derivatives in micelles. Colloids Surf A 167(3):253–262. doi:10.1016/S0927-7757(99)00313-1

Wang L, Wang M, Huang Z-H, Cui T, Gui X, Kang F, Wang K, Wu D (2011) Capacitive deionization of NaCl solutions using carbon nanotube sponge electrodes. J Mater Chem 21(45):18295–18299

Werner A, Konarev PV, Svergun DI, Hahn U (2009) Characterization of a fluorophore binding RNA aptamer by fluorescence correlation spectroscopy and small angle X-ray scattering. Anal Biochem 389(1):52–62. doi:10.1016/j.ab.2009.03.018